

# Electric dipole fields over an anisotropic seafloor: theory and application to the structure of 40 Ma Pacific Ocean lithosphere

Mark E. Everett<sup>1</sup> and Steven Constable<sup>2</sup>

<sup>1</sup> Department of Geology and Geophysics, Texas A & M University, College Station, TX 77843-3115, USA. E-mail: colt45@beerfrdg.tamu.edu

<sup>2</sup> Institute of Geophysics and Planetary Physics, Scripps Institution of Oceanography, La Jolla, CA 92093-0225, USA

Accepted 1998 July 20. Received 1998 July 6; in original form 1997 October 7

## SUMMARY

Seismic anisotropy has been detected in the oceanic crust and upper mantle, and likewise it is geologically reasonable to expect that a certain amount of lateral anisotropy exists in seafloor electrical properties. Anisotropy in Earth properties can often lead to surprising effects on geophysical responses that are not anticipated from simple isotropic theories. Here, we investigate the effects of lateral anisotropy on the frequency-domain, controlled-source electromagnetic (CSEM) response of a uniaxially conducting, non-magnetic seafloor excited by a horizontal electric dipole whose moment is oriented obliquely with respect to the electrical strike direction. A ‘paradox of anisotropy’ is observed, in which the seafloor electric field strength is enhanced in the most conductive direction of the seafloor. This enhancement is opposite to what one would expect based on naive isotropic theory. We also show that it is possible in certain circumstances to extract the along-strike electrical conductivity from marine controlled-source electromagnetic data using only isotropic modelling. The extraction of across-strike conductivity, however, requires full anisotropic modelling. The physical insight into electromagnetic induction in uniaxial media that is presented here should greatly assist the geological interpretation of marine CSEM experimental data. Applying our algorithm to the PEGASUS data set (CSEM data collected over 40 Ma Pacific Ocean lithosphere) produces a model with conductivity in the fossil spreading direction that is seven times greater than the conductivity perpendicular to spreading. Strain-aligned mineralogical fabric, as predicted by tectonic modelling, would explain our result, with enhanced conductivities caused by hydrogen conduction along the olivine *a*-axis or connected accumulations of trace conductors such as graphite or magnetite.

**Key words:** anisotropy, electrical conductivity, electromagnetic methods, marine geophysics.

## INTRODUCTION

In a seafloor controlled-source electromagnetic (CSEM) dipole–dipole experiment (e.g. Cox *et al.* 1986), a time-varying primary electric current is injected into the ocean basement using a deep-towed transmitter (TX). The variations in primary current cause eddy currents to flow in the conducting sea water and seafloor. The total electromagnetic field, which is the sum of the primary field due to the transmitter plus the secondary field generated by the eddy currents, is then detected by one or several receivers (RXs) that are either towed behind the transmitter or placed on the seafloor at various ranges. The high electrical conductivity of sea water, nominally  $3.2 \text{ S m}^{-1}$ , greatly attenuates the electromagnetic field in the frequency range 0.1–10 Hz (the skin depth, or e-folding distance, at 1 Hz is only 281 m). However, the electromagnetic field diffusing

through the more resistive seafloor propagates much further (the skin depth at 1 Hz for  $0.001 \text{ S m}^{-1}$  rocks is about 16 km). The electrical conductivity structure of oceanic mid-crustal and upper-mantle rocks is therefore determined by measuring the spatial dependence of the signal attenuation at these frequencies.

Theoretical calculations of the electromagnetic response of simple models to controlled-source excitation (Cheesman *et al.* 1987) have indicated that two TX/RX configurations are ideally suited for sounding of the seafloor: the directly coupled, horizontal electric dipole–dipole (HED) and the inductively coupled, horizontal magnetic dipole–dipole (HMD) systems. These two types have been extensively tested and developed in recent years: a magnetic dipole–dipole system operating in the time domain (Cheesman *et al.* 1993), and electric dipole–dipole systems operating in the time (Cairns *et al.* 1996) and

frequency domains (Cox *et al.* 1986; Sinha *et al.* 1990). The transient systems have found application in near-surface, high-resolution electrical studies of continental shelf sediments and hydrothermal sulphide deposits (Cairns *et al.* 1996; Evans *et al.* 1997). The frequency-domain HED system is better suited for deep crustal and upper-mantle studies since it generates larger induced electromagnetic fields, thus permitting greater TX/RX separations and a maximum depth of penetration into the Earth as much as 60 km (Constable & Cox 1996).

Following the first frequency-domain seafloor HED experiment conducted in 1980 (Young & Cox 1981), several other surveys of this type have been carried out. Two of these experiments studied the electrical conductivity depth profile of cool, mature oceanic crust and upper mantle in the North Pacific (Cox *et al.* 1986; Constable & Cox 1996) and found values typically between  $10^{-4}$  and  $10^{-5}$  S  $m^{-1}$  over the approximate depth range 10–30 km. Three other experiments, like the original, were targeted at mid-ocean-ridge crustal structure (Evans *et al.* 1994; MacGregor *et al.* 1998; Sinha *et al.* 1996).

The field experiments have driven the development of interpretational tools. A forward modelling algorithm (Chave & Cox 1982; Chave 1983) has long been available for the computation of seafloor electromagnetic fields generated by vertical and horizontal current sources in the conducting ocean overlying a 1-D earth. This algorithm has recently been improved and combined with the regularized inversion strategy of Constable *et al.* (1987) to provide an efficient means

of generating smoothly varying 1-D electrical conductivity profiles that are consistent with observed responses (Flosadottir & Constable 1996). A pair of finite element algorithms now exist for computing the electromagnetic fields due to an HED source deployed on or near a 2-D conducting seafloor: one is in the time domain (Everett & Edwards 1992) while the other is in the frequency domain (Unsworth *et al.* 1993). Unsworth & Oldenburg (1995) used the frequency-domain finite element code to develop an efficient, approximate method for regularized inversion of marine controlled-source data in terms of a 2-D electrical conductivity model.

The purpose of our paper is to study the effect of horizontal anisotropy in the seafloor crust and uppermost mantle on a frequency-domain experiment. Our efforts are motivated by data from the PEGASUS experiment of Constable & Cox (1996). These data are shown in Fig. 1, along with a map of the experimental layout and the available swath bathymetry for this area of the Northeast Pacific ocean basin. The fossil ridge-parallel direction is echoed by the predominantly N–S bathymetric fabric, as shown. The experiment was designed with possible seafloor electrical anisotropy in mind, hence the HED transmitter was towed at an azimuth of  $135^\circ$  with respect to the bathymetric fabric and the instruments were laid out in both across-strike and along-strike directions from the transmitter. The amplitudes of the observed long-range (>30 km) horizontal electric field depend systematically not on signal-propagation direction as might be expected, but instead on the orientation of the receiver with respect to the predominant

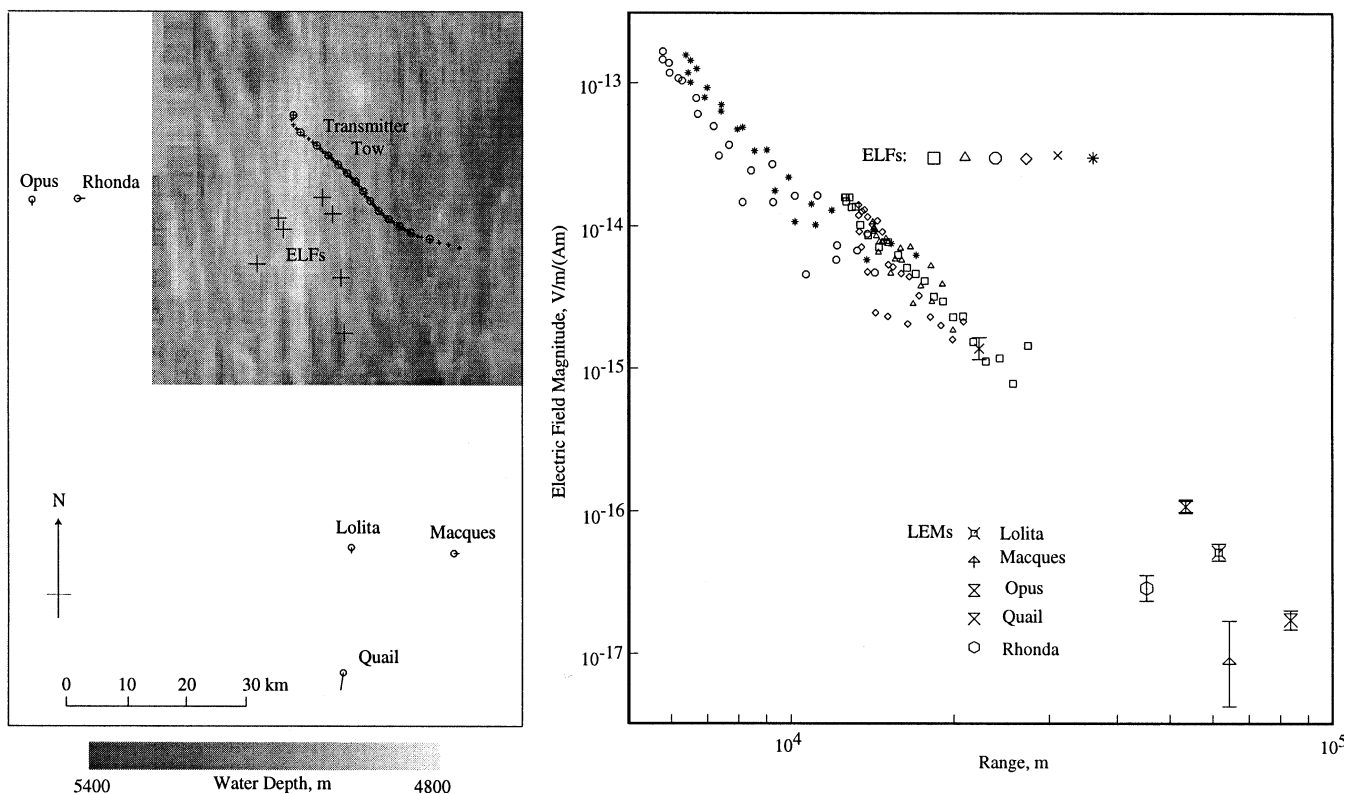


**Figure 1.** Left: map view of the available swath bathymetry and instrument layout of the PEGASUS frequency-domain CSEM experiment in the Northeast Pacific Ocean. The bottom left corner of the map is at  $34.5^\circ\text{N}$ ,  $132.5^\circ\text{W}$ . Seafloor electric field sensors Lolita, Opus and Quail have N–S-oriented antennae, as indicated by the symbols, and thus measure the N–S component of the electric field generated by the horizontal electric dipole transmitter. Likewise, sensors Rhonda and Macques measure the E–W component of the electric field. Right: the observed electric field magnitude as a function of TX–RX separation distance for the various short-range ('ELFs') and long-range ('LEMs') seafloor instruments.

strike of the bathymetric fabric. Instruments Lolita, Opus and Quail, with N–S-oriented antennae, record electric fields that are about four times larger for a given range than those recorded by instruments Rhonda and Macques, which have E–W-oriented antennae.

Although the PEGASUS data coverage is certainly limited, one might speculate that these systematics are caused by horizontal anisotropy in seafloor electrical conductivity. Seismic anisotropy has previously been detected (Shearer & Orcutt 1985) both in the oceanic crust, associated with fracturing and dykes, and in the oceanic mantle, thought to be associated with the preferential orientation of olivine crystallographic axes (Zhang & Karato 1995).

Yu & Edwards (1992) describe a general theory for calculating the transient response of a laterally anisotropic seafloor to excitation by arbitrary electric or magnetic sources located in sea water. They present calculations of the transient response for electric and magnetic field sensors (RX) located in line with and perpendicular to the moment of an HED transmitter (TX). The latter, in turn, is presumed to be oriented parallel or perpendicular to the strike of the electrical conductivity. Yu *et al.* (1997) extend the calculations to the case of a triaxially anisotropic seafloor. In this contribution, we study the frequency-domain response of a horizontally anisotropic seafloor excited by an HED transmitter whose moment is obliquely oriented with respect to the strike of the anisotropy. The results presented here are of practical use since most of the existing seafloor CSEM data are in the frequency domain. In addition, the experimental geometry invariably deviates from the ideal case of TX moment and RXs aligned with the principal conductivity axes, which in general are not known *a priori*.

The effects of lateral electrical anisotropy on dipole fields are also of interest in surface and borehole CSEM applications. For example, the electromagnetic response of a laterally anisotropic half-space to surface dipole transmitters has been studied by Le Masne & Vasseur (1981) and more recently by Li & Pedersen (1991). The response of a dipole embedded within an anisotropic whole-space was first solved some years ago (Clemmow 1963) by appropriately scaling the free-space dipole response. Xiong (1989) has since calculated the field of a dipole embedded in a stratified anisotropic earth.

## UNIAXIAL ELECTRICAL CONDUCTIVITY

We will discuss the general case of the seafloor HED sounding system in Cartesian geometry as shown in Fig. 2. The transmitter antenna is deployed on or near the seafloor  $z=0$  with its moment directed at some arbitrary angle  $\phi$ , measured positive clockwise with respect to the Cartesian  $y$  direction. Electric and magnetic receivers are placed at various ranges and azimuths with respect to the direction of the HED moment. The vertical coordinate  $z$  is measured positive downwards. The anisotropic electrical conductivity of the lower half-space ( $z > 0$ ) is given by the diagonal tensor:

$$\sigma = \begin{pmatrix} \sigma_x & & \\ & \sigma_y & \\ & & \sigma_z \end{pmatrix}. \quad (1)$$

In the isotropic case,  $\sigma_x = \sigma_y = \sigma_z$ . In this contribution we consider only a ‘uniaxial’ conducting seafloor in which one of

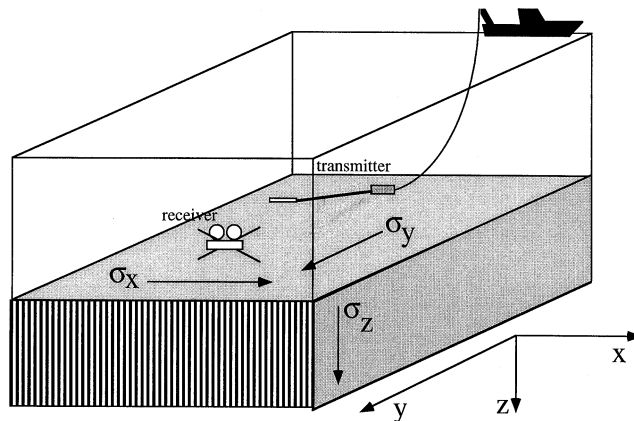


**Figure 2.** A marine controlled-source electromagnetic (CSEM) experiment over a uniaxial seafloor. The horizontal electric dipole (HED) transmitter, oriented at some oblique angle with respect to the electric strike direction  $y$ , is towed along the seafloor, while orthogonal pairs of horizontal electric fields are measured by seafloor receivers located at various ranges and azimuths from the transmitter.

the components of the conductivity tensor is different from the other two. Hereafter, we define the strike direction to be the direction (either  $x$  or  $y$ ) in which the horizontal conductivity is equal to the vertical conductivity. The electrical conductivity  $\sigma_0$  of the upper half-space ( $z < 0$ ) is assumed to be isotropic.

The possible electrical materials that can be described by a uniaxial conductivity tensor include two orthogonal types of horizontally anisotropic media, characterized respectively by the tensors  $\sigma = \text{diag}(\sigma_{\perp}, \sigma_{\parallel}, \sigma_{\parallel})$  and  $\sigma = \text{diag}(\sigma_{\parallel}, \sigma_{\perp}, \sigma_{\parallel})$ , in addition to a vertically anisotropic medium characterized by the tensor  $\sigma = \text{diag}(\sigma_{\parallel}, \sigma_{\parallel}, \sigma_{\perp})$ . It is worthwhile to review the various physical realizations of a uniaxial electrically conducting medium (Fig. 3). In principle, the media shown can be fabricated by impregnating conducting rods or sheets (shaded regions) within a less conductive matrix (white regions). For a given type of anisotropy, the shape and orientation of the conductors determines the relative size of the quantities  $\sigma_{\parallel}$  and  $\sigma_{\perp}$ . For example, consider a vertically anisotropic material (bottom row of Fig. 3). The case  $\sigma_{\parallel} > \sigma_{\perp}$  corresponds to horizontally aligned conductive sheets. Beneath the seafloor, this geometry corresponds to an idealized representation of fine-scale, interbedded geological strata. The other case,  $\sigma_{\parallel} < \sigma_{\perp}$ , is generated by vertically aligned conductive rods, which is an unusual geometry but might be applicable to diapiric upwelling of melt in a volcanic system. There is no strike direction associated with a vertically anisotropic medium.

The horizontal cases (top two rows of Fig. 3) are equivalent except for the strike direction (as defined by the vertical conductivity), which differs by  $90^\circ$ . This means that if the electromagnetic field is known for an arbitrary excitation of one type of horizontally anisotropic medium, the field for the same excitation of the orthogonal type is found by simply rotating the coordinates through  $90^\circ$ . It therefore suffices to consider just the top row in Fig. 3. As shown in the figure, the case  $\sigma_{\parallel} > \sigma_{\perp}$  is generated by vertically aligned conductive sheets, a geometry that is associated with dykes and fractures, which are commonly found in oceanic crust. The case  $\sigma_{\parallel} < \sigma_{\perp}$  corresponds to horizontally aligned conductive rods, which is an idealized geometric model for the ‘lattice preferred

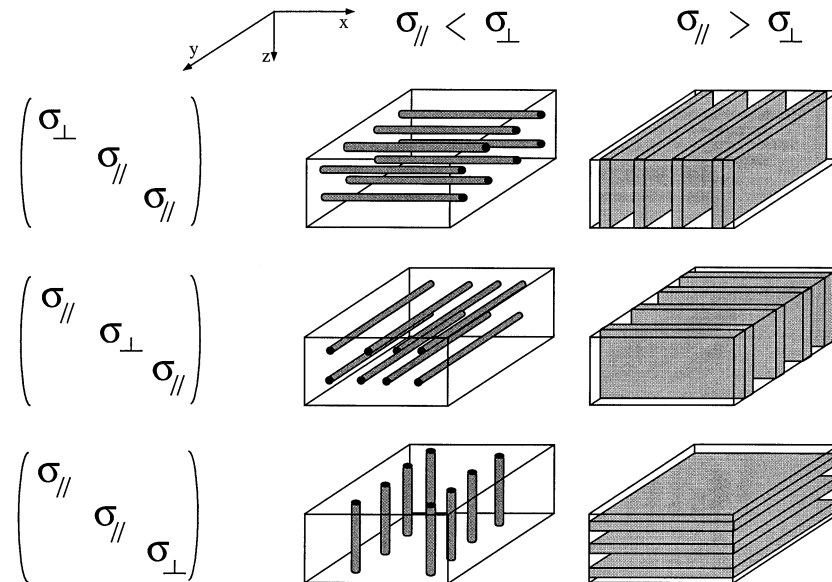


**Figure 3.** Physical realizations of a medium characterized by a uniaxial electrical conductivity tensor. The realizations shown may in principle be fabricated by impregnating conductors (shaded regions) within an insulating matrix (white regions). We define the strike direction to be the direction (either  $x$  or  $y$ ) in which the horizontal conductivity is equal to the vertical conductivity; thus, strike is in the  $y$ -direction in the top row of structures, and in the  $x$ -direction in the middle row. Notice that this definition of strike could conflict with a geologist's definition.

orientation' of olivine aggregates that results from stress-induced deformation of the upper mantle (Zhang & Karato 1995). Horizontal rods are also consistent with the occurrence of organized conductive lineaments of  $\sim 1$ – $10$  km length that we hypothesize might form during rifting of the upper mantle beneath a mid-ocean ridge. It is interesting to note that, according to our previous definition, the 'electrical strike' of the medium shown in the top left of Fig. 3 is in the  $y$ -direction, even though strike to a geologist would appear to be in the  $x$ -direction.

## ANALYTICAL RESULTS

The bulk electrical conductivity of the oceanic crust and uppermost mantle, measured at the frequencies (0.1 Hz–1 kHz) and TX–RX separations (1–100 km) typical of a deep-probing marine CSEM experiment, is 1–5 orders of magnitude less than that of the overlying sea water (Cox *et al.* 1986). At these frequencies and ranges, owing to the skin effect, there is little electric current flow in the sea water. Hence, the vertical electric field strength that would be measured by a seafloor RX in a typical experiment is negligible compared to the horizontal field strength. In most experiments, therefore, just the orthogonal horizontal electric fields are measured.

In marine electromagnetics, it is conventional both in theory (Chave & Cox 1982) and in practice (Constable & Cox 1996) to decompose the horizontal electric field at the seafloor into radial  $E_\rho$  and azimuthal  $E_\phi$  components. This decomposition reflects the natural azimuthal symmetry of an isotropic seafloor. However, if the electrical conductivity of the seafloor is horizontally anisotropic, it is more advantageous (Yu & Edwards 1992) to decompose the horizontal field into components that are aligned parallel and perpendicular to the electrical strike direction. Such a decomposition permits an easier theoretical evaluation of the fields. In addition, we

expect that the across-/along-strike components are better diagnostics of seafloor lateral anisotropy than their radial/azimuthal counterparts.

In this section we calculate the seafloor horizontal electric field generated by an HED transmitter whose moment is oriented at an arbitrary angle  $\phi$  with respect to the strike of a uniaxial, non-magnetic lower half-space. The latter is characterized by the electrical conductivity tensor  $\sigma = \text{diag}(\sigma_\perp, \sigma_\parallel, \sigma_\parallel)$ . The asymmetry of electrical conductivity in the  $x$  and  $y$  horizontal directions in this type of medium precludes the use of Hankel transforms to obtain an analytic formula for the electric field. Instead, it proves convenient (Yu & Edwards 1992) to solve for the horizontal electric field components  $e_x, e_y$  directly in the 2-D Fourier wavenumber domain ( $p, q$ ). Following this, double-sine and double-cosine transforms are invoked to recover the across-/along-strike field components  $E_x, E_y$  in the spatial ( $x, y$ ) domain.

The 2-D Fourier transform pair for an arbitrary function is defined by

$$f(p, q) = \int_{-\infty}^{\infty} \int_{-\infty}^{\infty} F(x, y) \exp(+ipx + iqy) dx dy, \quad (2)$$

$$F(x, y) = \frac{1}{4\pi^2} \int_{-\infty}^{\infty} \int_{-\infty}^{\infty} f(p, q) \exp(-ipx - iqy) dp dq. \quad (3)$$

Lower-case symbols are used throughout the paper to denote EM field components in the double-wavenumber domain while upper-case symbols are used for components in the spatial domain.

Seafloor CSEM experiments are carried out at sufficiently low frequencies (up to 1 kHz, or thereabouts, for even the most shallow-probing experiments) that the electromagnetic energy transport mechanism through the sea water and underlying crust is due to diffusion rather than the familiar wave propagation applicable at higher frequencies. The governing Maxwell equations for time-harmonic excitation of the form

$\exp(+i\omega t)$  in the low-frequency regime are thus Faraday's law,

$$\nabla \times \mathbf{E} = -i\omega \mathbf{B}, \quad (4)$$

and Ampere's law,

$$\nabla \times \mathbf{B} = \mu_0 \sigma \mathbf{E} + \mu_0 \mathbf{J}_S, \quad (5)$$

where  $\omega$  is angular frequency,  $\mu_0$  is the magnetic permeability of free space, and  $\mathbf{J}_S$  describes the electric current density of the source. In addition, the magnetic field is divergence-free  $\nabla \cdot \mathbf{B} = 0$  and the electric field satisfies the continuity equation  $\nabla \cdot (\sigma \mathbf{E}) = 0$  to ensure conservation of electric charge.

Combining eqs (4) and (5) in source-free ( $\mathbf{J}_S = 0$ ) regions results in the vector diffusion equation

$$\nabla \times \nabla \times \mathbf{E} + i\omega \mu_0 \sigma \mathbf{E} = 0. \quad (6)$$

This equation is valid inside the lower half-space only since the HED source is located in the upper half-space. Following Yu & Edwards (1992), the condition  $\partial/\partial x[\nabla \cdot (\sigma \mathbf{E})] = 0$  [which follows directly from continuity equation  $\nabla \cdot (\sigma \mathbf{E}) = 0$ ] is applied to the  $x$ -component of the vector diffusion equation (6). Explicitly, the continuity condition  $\partial/\partial x[\nabla \cdot (\sigma \mathbf{E})] = 0$  for the particular choice of conductivity tensor  $\sigma = \text{diag}(\sigma_{\perp}, \sigma_{\parallel}, \sigma_{\parallel})$  is

$$-\frac{\sigma_{\perp}}{\sigma_{\parallel}} \frac{\partial^2 E_x}{\partial x^2} = \frac{\partial^2 E_y}{\partial x \partial y} + \frac{\partial^2 E_z}{\partial x \partial z}.$$

The left-hand side of this expression then replaces the first two terms of the  $x$ -component of the vector diffusion equation (6), which written explicitly is

$$\frac{\partial^2 E_y}{\partial x \partial y} + \frac{\partial^2 E_z}{\partial x \partial z} - \frac{\partial^2 E_x}{\partial y^2} - \frac{\partial^2 E_x}{\partial z^2} + i\omega \mu_0 \sigma_{\perp} E_x = 0.$$

There results the following *scalar* partial differential equation (PDE), which is satisfied by the across-strike component  $E_x$  of the electric field:

$$-\frac{\sigma_{\perp}}{\sigma_{\parallel}} \frac{\partial^2 E_x}{\partial x^2} - \frac{\partial^2 E_x}{\partial y^2} - \frac{\partial^2 E_x}{\partial z^2} + i\omega \mu_0 \sigma_{\perp} E_x = 0. \quad (7)$$

This PDE can be solved with a 2-D Fourier transform in the  $x$ - and  $y$ -directions. Recognizing that second-order derivatives  $\partial^2/\partial x^2$  and  $\partial^2/\partial y^2$  in the spatial domain correspond to multiplications in the wavenumber domain by  $-p^2$  and  $-q^2$ , respectively, there results the ordinary differential equation (ODE)

$$\frac{d^2 e_x}{dz^2} - v_2^2 e_x = 0, \quad (8)$$

where  $v_2 \equiv \sqrt{(\sigma_{\perp} p^2 / \sigma_{\parallel} + q^2 + i\omega \mu_0 \sigma_{\perp})}$  has been defined.

A similar ODE can be derived for the across-strike magnetic field component. Eliminating the electric field vector  $\mathbf{E}$  from Ampere's law (4) and Faraday's law (5) results in a second vector diffusion equation,

$$\nabla \times \sigma^{-1} \nabla \times \mathbf{B} + i\omega \mu_0 \mathbf{B} = 0, \quad (9)$$

where the inverse of the electrical conductivity tensor is  $\sigma^{-1} = \text{diag}(\sigma_{\perp}^{-1}, \sigma_{\parallel}^{-1}, \sigma_{\parallel}^{-1})$ . Next, the  $x$ -derivative of the divergence-free condition  $\nabla \cdot \mathbf{B} = 0$  is applied to the  $x$ -component of the vector diffusion equation (9), resulting in the following PDE for the across-strike magnetic field:

$$-\frac{\partial^2 B_x}{\partial x^2} - \frac{\partial^2 B_x}{\partial y^2} - \frac{\partial^2 B_x}{\partial z^2} + i\omega \mu_0 \sigma_{\parallel} B_x = 0. \quad (10)$$

Taking a 2-D Fourier transform, as before, results in the ODE

$$\frac{d^2 b_x}{dz^2} - v_1^2 b_x = 0, \quad (11)$$

where  $v_1 \equiv \sqrt{(p^2 + q^2 + i\omega \mu_0 \sigma_{\parallel})}$  has been defined.

Eqs (8) and (11) constitute a pair of ODEs that govern the behaviour of the across-strike electromagnetic field components  $e_x, b_x$  inside the uniaxial medium, beneath the seafloor. A similar pair of equations can be derived that are valid in the overlying isotropic half-space representing the ocean. However, the HED source (TX) is located at height  $h$  above the seafloor, as shown in Fig. 4, and needs to be included in the upper-half-space solutions. The EM field components  $e_x, b_x$  in isotropic medium 0, located below the transmitter but above the seafloor, consequently have the form

$$e_x^0(p, q) = C_1 \exp(-v_0 z) + G \exp(v_0 z), \quad (12)$$

$$b_x^0(p, q) = C_2 \exp(-v_0 z) + H \exp(v_0 z), \quad (13)$$

where  $v_0 \equiv \sqrt{(p^2 + q^2 + i\omega \mu_0 \sigma_0)}$ . The source terms  $C_1, C_2$  are known and describe the downward diffusion of the EM field from the TX to the seafloor. The coefficients  $G$  and  $H$  characterize the upwardly diffusing fields that are due to 'reflections' from the uniaxial seafloor. They are unknowns that will be found by the application of boundary conditions. Beneath the seafloor, the EM fields are decaying solutions to the governing equations (8) and (11), namely

$$e_x^1(p, q) = U \exp(-v_2 z), \quad (14)$$

$$b_x^1(p, q) = V \exp(-v_1 z). \quad (15)$$

The coefficients  $U$  and  $V$  are also unknowns and are due to 'transmission' of the EM fields into the uniaxial seafloor. It is interesting to note that  $e_x$  and  $b_x$  have different characteristic decay lengths into the seafloor, a consequence of the anisotropy.

At the seafloor  $z=0$ , the tangential EM field components  $e_x, b_x, e_y$  and  $b_y$  must be continuous. Enforcing the continuity of the across-strike components  $e_x$  and  $b_x$  is simple. From the previously developed equations it follows that  $C_1 + G = U$  and  $C_2 + H = V$ . To apply continuity of the along-strike coefficients  $e_y$  and  $b_y$ , it is first necessary to find expressions for these quantities in terms of the across-strike components  $e_x$  and

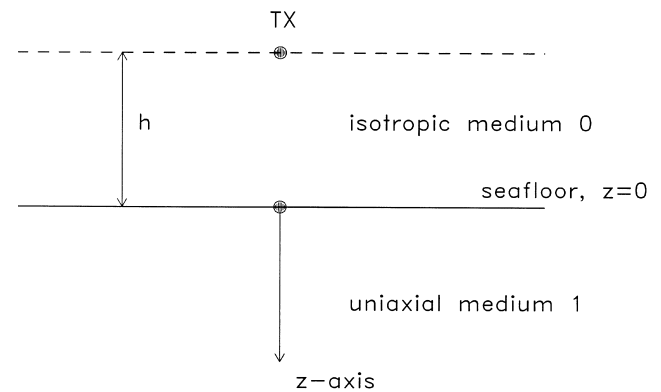


**Figure 4.** Sketch showing the location of the transmitter (TX) relative to the seafloor. The TX is located at height  $h$  above the seafloor during the development of the analytic solution. For the numerical calculations in this paper, the TX is moved to the seafloor ( $h=0$ ).

$b_x$ . This is accomplished by the following manipulations of Maxwell equations (Yu & Edwards 1992). Multiplying the  $y$ -component of Ampere's law (4) by  $i\omega$  and eliminating  $B_z$  by invoking the  $x$ -derivative of the  $z$ -component of Faraday's law (5), and taking a 2-D Fourier transform of the resulting equation, one obtains

$$e_y^0(p, q) = \frac{1}{p^2 + i\omega\mu_0\sigma_0} \left( pqe_x^0 + i\omega \frac{\partial b_x^0}{\partial z} \right). \quad (16)$$

The analogous expression for the along-strike electric field  $e_y^1(p, q)$  beneath the seafloor is obtained by substituting in eq. (16) superscript '1' for superscript '0' and replacing  $\sigma_0$  with  $\sigma_{\parallel}$ . Equating  $e_y^0$  with  $e_y^1$  at the seafloor yields the sought-after constraint:

$$\begin{aligned} & \frac{1}{p^2 + i\omega\mu_0\sigma_0} \{pq(C_1 + G) + i\omega(-v_0C_2 + v_0H)\} \\ &= \frac{1}{p^2 + i\omega\mu_0\sigma_{\parallel}} \{pqU - i\omega v_1V\}. \end{aligned} \quad (17)$$

Next, multiplying the  $y$ -component of Faraday's law (5) by  $-\mu_0\sigma_{\parallel}$  and eliminating  $E_z$  by invoking the  $x$ -derivative of the  $z$ -component of Ampere's law (4), and taking a 2-D Fourier transform of the resulting equation, one obtains

$$b_y^0(p, q) = \frac{1}{p^2 + i\omega\mu_0\sigma_0} \left( pqb_x^0 - \mu_0\sigma_0 \frac{\partial e_x^0}{\partial z} \right). \quad (18)$$

The analogous expression for the across-strike magnetic field  $b_y^1(p, q)$  beneath the seafloor is obtained by substituting in eq. (18) superscript '1' for superscript '0' and replacing  $\sigma_0$  with  $\sigma_{\parallel}$ . Equating  $b_y^0$  with  $b_y^1$  at the seafloor yields the final constraint:

$$\begin{aligned} & \frac{1}{p^2 + i\omega\mu_0\sigma_0} \{pq(C_2 + H) - \mu_0\sigma_0(-v_0C_1 + v_0G)\} \\ &= \frac{1}{p^2 + i\omega\mu_0\sigma_{\parallel}} \{pqV + \mu_0\sigma_0v_2U\}. \end{aligned} \quad (19)$$

There are now four linear constraint equations in the four unknown coefficients  $G, H, U, V$ . The quantities  $C_1$  and  $C_2$  are known and depend on the orientation of the HED dipole moment with respect to the strike of the anisotropy, as will be indicated later. The analytic solution to the  $4 \times 4$  linear system of constraint equations is

$$U = \frac{-2i\omega v_0 w_1^2}{\Lambda} [\mu_0\sigma_0 C_1(v_0 w_1^2 + v_1 w_0^2) + pqC_2(w_1^2 - w_0^2)], \quad (20)$$

$$V = \frac{-2\mu_0 v_0 w_1^2}{\Lambda} [-pq\sigma_0 C_1(w_1^2 - w_0^2) + i\omega C_2(\sigma_0 v_0 w_1^2 + \sigma_{\parallel} v_2 w_0^2)], \quad (21)$$

where

$$\Lambda \equiv -i\omega\mu_0(v_0 w_1^2 + v_1 w_0^2)(\sigma_0 v_0 w_1^2 + \sigma_{\parallel} v_2 w_0^2) - p^2 q^2 (w_1^2 - w_0^2)^2 \quad (22)$$

and  $w_0^2 = p^2 + i\omega\mu_0\sigma_0$ ,  $w_1^2 = p^2 + i\omega\mu_0\sigma_{\parallel}$ . The problem is now basically solved, except for the specification of the source terms  $C_1$  and  $C_2$ . These can be deduced by comparison of eqs (12) and (13) with the  $p, q$ -wavenumber domain expressions for the EM field of an electric dipole in a whole-space (Kaufmann & Keller 1983). For an arbitrarily oriented HED transmitter of moment

$P$  located on the seafloor ( $h=0$ ), the source terms are

$$C_1 = \frac{-Pw_0^2}{2\sigma_0 v_0} \sin \phi - \frac{pqP}{2\sigma_0 v_0} \cos \phi \quad (23)$$

and

$$C_2 = \frac{\mu_0 P}{2} \cos \phi. \quad (24)$$

The angle  $\phi$  is measured positive clockwise with respect to the strike direction  $y$  of the uniaxial seafloor.

The horizontal electric field components  $e_x(p, q)$  and  $e_y(p, q)$  in the  $p, q$ -wavenumber domain can now be assembled using the previously developed equations. Once this is done, the spatial variations of the horizontal electric field are recovered by invoking 2-D inverse Fourier transforms of the resulting wavenumber domain expressions for  $e_x(p, q)$  and  $e_y(p, q)$ . A simplification can be made since each of the latter decompose into a sum of two terms: one that is even in  $p, q$  and one that is odd in  $p, q$ . In such cases, the 2-D inverse Fourier transform of the even function of  $p, q$  reduces to a double-cosine transform, while that of an odd function of  $p, q$  reduces to a double-sine transform. The algebraic manipulation required to obtain  $E_x(x, y)$  and  $E_y(x, y)$  according to these procedures is straightforward but too lengthy to reproduce here. However, the final expressions are quite simply

$$\begin{aligned} E_x(x, y) &= \frac{i\omega\mu_0 P}{\pi^2} \int_0^{\infty} \int_0^{\infty} \frac{dp dq}{\Lambda} \\ &\times [a_1(p, q) \cos px \cos qy + a_2(p, q) \sin px \sin qy dpdq], \end{aligned} \quad (25)$$

$$\begin{aligned} E_y(x, y) &= \frac{i\omega\mu_0 P}{\pi^2} \int_0^{\infty} \int_0^{\infty} \frac{dp dq}{\Lambda} \\ &\times [a_3(p, q) \cos px \cos qy + a_4(p, q) \sin px \sin qy dpdq], \end{aligned} \quad (26)$$

where the double-cosine and double-sine kernels are given by

$$\begin{aligned} a_1(p, q) &= w_0^2 w_1^2 (v_0 w_1^2 + v_1 w_0^2) \sin \phi, \\ a_2(p, q) &= pq w_0^2 w_1^2 (v_0 + v_1) \cos \phi, \\ a_3(p, q) &= -p^2 q^2 (v_0 w_0^2 + v_1 w_1^2) \cos \phi \\ &\quad - i\omega\mu_0 v_0 v_1 (\sigma_{\parallel} v_2 w_0^2 + \sigma_0 v_0 w_1^2) \cos \phi, \\ a_4(p, q) &= pq w_0^2 w_1^2 (v_0 + v_1) \sin \phi. \end{aligned} \quad (27)$$

In summary, eqs (25) and (26) constitute formulae for the horizontal electric field on the seafloor that is generated by an oscillating, arbitrarily oriented HED source of dipole moment  $P$ . The source is located on the seafloor, which in turn is characterized by a uniaxial conductivity tensor  $\sigma = \text{diag}(\sigma_{\perp}, \sigma_{\parallel}, \sigma_{\parallel})$ . The formulae (25–26) are indispensable if frequency-domain marine electric dipole–dipole experiments (e.g. Constable & Cox 1996) are to be interpreted in terms of horizontally anisotropic electrical structure. Also, the closed-form nature of the formulae facilitates an investigation into the physics of electromagnetic induction in uniaxial media. The effect of lateral anisotropy on seafloor horizontal electric fields is examined in the next section of the paper, with some surprising results.

## NUMERICAL RESULTS

For the examples presented here, the HED transmitter dipole moment is assumed to be oriented at  $\phi=135^\circ$  with respect to strike, the positive- $y$  direction. This TX orientation was chosen since it is the dominant geometry in the PEGASUS experiment (Constable & Cox 1996), at least under the gross assumption that the preferentially aligned N–S bathymetric fabric of the Northeast Pacific ocean basin reflects an underlying uniaxial half-space whose electrical strike is also directed north–south. This assumption may not be true since the electrical strike direction, if one exists, may instead be governed by mantle flow processes or current Pacific plate-motion directions, neither of which trend north–south. However, the orientation  $\phi=135^\circ$  represents a sufficiently general case for which to evaluate the behaviour of seafloor fields.

In the present paper, the double-cosine and double-sine transforms in eqs (25–26) were evaluated using the continued-fraction method of Chave (1983). The integrals over the  $q$ -wavenumber were performed first, for a fixed number  $n_p$  of values of the  $p$ -wavenumber, the latter being logarithmically spaced between  $p_{\min}$  and  $p_{\max}$ . The results of the  $q$ -integrals were then treated as functions of  $p$  and splined. The integrals over  $p$  were then evaluated using again the method of Chave (1983), with the splined functions acting as the kernels. For the modelling in this paper, we found that  $p_{\min}=10^{-8}$  and  $p_{\max}=100$  yielded accurate results. After some numerical experimentation, the number of  $p$ -values was set to  $n_p=180$ , which ensured a high accuracy of the resulting electric fields everywhere they were calculated in the  $x/y$ -plane. However, it was found that at some locations as few as 25  $p$ -values would have sufficed. In general, the largest number of  $p$ -wavenumbers are required when evaluating the electric fields at  $|x/y|\gg 1$  or  $|x/y|\ll 1$ , while the lowest number are required at  $|x|\sim|y|$ . L. Yu (personal communication, 1997) recommends the following approach if computational efficiency becomes an issue: if  $x$  is larger than  $y$ , perform the  $p$ -integration first; otherwise, reverse the order.

A plan view of the seafloor is shown in Fig. 5, indicating the orientation of the HED transmitter and some profiles along which the electric field is to be evaluated. Fig. 6 contains profiles of the complex seafloor electric field components along

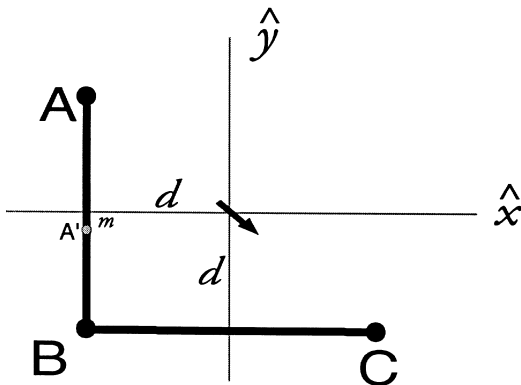


**Figure 5.** A plan view of the seafloor showing the orientation of the HED transmitter with respect to the  $y$ -axis, the electrical strike direction. Electric fields are calculated along profiles A–A', A–B and B–C.

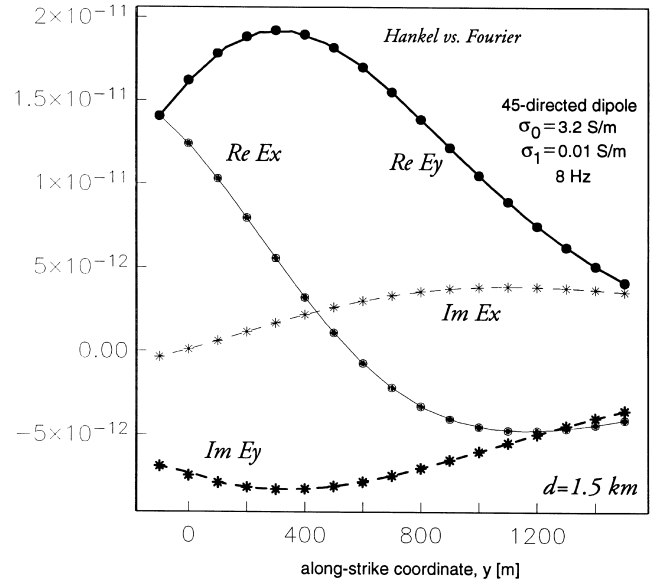


**Figure 6.** A comparison of complex electric field components along the profile A–A' shown in Fig. 5 for a  $135^\circ$ -directed dipole. The solid lines are the field components calculated using the isotropic Hankel transform expressions of Chave & Cox (1982). The symbols are the field components calculated using the anisotropic double-sine/cosine transform expressions (25–26) developed in this paper. The model parameters are indicated in the legend.

the line A–A' indicated in Fig. 5. These results, like all others in the paper except where noted, are for 8 Hz frequency ( $\omega=50.26 \text{ rad s}^{-1}$ ) and isotropic upper-half-space electrical conductivity  $\sigma_0=3.2 \text{ S m}^{-1}$ . For the profiles in Fig. 6, the lower half-space is also isotropic, with electrical conductivity  $\sigma_1=0.01 \text{ S m}^{-1}$ . The TX–RX separations range between 1.5 and 2.1 km along the line A–A', corresponding to 15–20 skin depths in the sea water and  $\sim 1.2$  skin depths in the seafloor. The electric field for this geometry can be expressed in closed form (Chave & Cox 1982) in terms of Hankel transforms. The solid lines in Fig. 6 are the complex field components calculated using the Hankel transform formulae

$$E_x(x, y) = \frac{P}{2\sqrt{2\pi}} \int_0^\infty d\lambda \left[ J_0(\lambda\rho) \left\{ -\frac{i\mu_0\omega\lambda}{u_0+u_1} - \frac{\lambda^3 x(x+y)}{\rho^2(\sigma_0 u_1 + \sigma_1 u_0)} \right\} + J_1(\lambda\rho) \left\{ \frac{\lambda^2(x^2 + 2xy - y^2)}{\rho^3(\sigma_0 u_1 + \sigma_1 u_0)} \right\} \right], \quad (28)$$

$$E_y(x, y) = \frac{P}{2\sqrt{2\pi}} \int_0^\infty d\lambda \left[ J_0(\lambda\rho) \left\{ \frac{i\mu_0\omega\lambda}{u_0+u_1} + \frac{\lambda^3 y(y+x)}{\rho^2(\sigma_0 u_1 + \sigma_1 u_0)} \right\} + J_1(\lambda\rho) \left\{ \frac{\lambda^2(x^2 - 2xy - y^2)}{\rho^3(\sigma_0 u_1 + \sigma_1 u_0)} \right\} \right], \quad (29)$$

where  $\rho = \sqrt{x^2 + y^2}$ ,  $u_0 = \sqrt{\lambda^2 + i\mu_0\omega\sigma_0}$ ,  $u_1 = \sqrt{\lambda^2 + i\mu_0\omega\sigma_1}$  and  $J_0, J_1$  are Bessel functions. The symbols in Fig. 6 represent the field components calculated using eqs (25–26). The excellent agreement between the two methods of calculation shows that the ‘anisotropic formulae’ (25–26) and our computation of them properly reduce to the Hankel transform formulae (28–29) in the isotropic limit.

### The $x$ -directed rods model

As previously mentioned, a uniaxial seafloor characterized by the electrical conductivity tensor  $\sigma = \text{diag}(\sigma_{\perp}, \sigma_{\parallel}, \sigma_{\parallel})$  with  $\sigma_{\parallel} < \sigma_{\perp}$  has the physical interpretation of  $x$ -directed conductive rods impregnating an insulating matrix (top left of Fig. 3). This geometry is associated in the upper mantle with either ‘lattice preferred orientation’ of olivine aggregates or spatially organized conductive lineaments. The anisotropy ratio  $f = \sigma_{\perp} / \sigma_{\parallel}$  in the upper mantle is unknown, but values as high as 10 could be geologically reasonable.

The magnitude of the seafloor across-strike electric field  $\log_{10}|E_x(x, y)|$  for an ‘ $x$ -directed rods’ model with anisotropy ratio  $f = 10$  is indicated in Fig. 7(a). The contour plot spans an area of seafloor that is 60 km  $\times$  60 km and is centred on the transmitter. Contours of  $\log_{10}|E_x|$  are shown for an  $x$ -directed rods model (light solid lines) with  $\sigma_{\perp} = 0.001 \text{ S m}^{-1}$  and  $\sigma_{\parallel} = 0.0001 \text{ S m}^{-1}$ , along with those for an isotropic seafloor model (heavy dashed lines) with  $\sigma_1 = \sigma_{\parallel} = 0.0001 \text{ S m}^{-1}$ . The contours of the along-strike component,  $\log_{10}|E_y|$ , and the total electric field,  $\log_{10}|E|$ , amplitudes for the same models are shown in Figs 7(b) and (c), respectively.

From Fig. 7(a), a comparison of the two sets of contour lines reveals that the across-strike electric field  $|E_x|$  close to the  $x$ -axis (in other words,  $y \sim 0$ ) is greater for the  $x$ -directed rods model (solid lines) than for the background isotropic model (dashed lines). This effect is shown again in the bottom panel of Fig. 8, which displays profiles of  $\log_{10}|E_x|$  along the line A–B–C (indicated in Fig. 5) for the  $x$ -directed rods (asterisks) and the two relevant background isotropic models (solid lines). Notice in Fig. 8, at the location  $y \sim 0$  halfway along the line A–B, that the quantity  $|E_x|$  associated with the  $x$ -directed rods model (asterisks) is *larger* than that associated with either of the background isotropic models. However, one would naively expect that the quantity  $|E_x|$  should be *smaller* at  $y \sim 0$  because to get there the EM fields must have diffused from the TX along the  $x$ -axis, which is the most conductive and thus dissipative direction available. In isotropic media, EM field attenuation increases with electrical conductivity according to the skin effect. In laterally anisotropic media, it seems that attenuation should therefore be greatest in the conductive direction and least in the resistive direction. However, the opposite effect is true: attenuation is least in the most conductive direction. This surprising, non-intuitive result is a ‘paradox of anisotropy’.

From Fig. 7(b) it is evident that the along-strike electric field strength  $|E_y|$  contours for the  $x$ -directed rods model (solid lines) follow almost exactly the field-strength contours for the isotropic half-space model (dashed lines), where the isotropic conductivity is  $\sigma_1 = \sigma_{\parallel} = 0.0001 \text{ S m}^{-1}$ . This is clearly shown in the top panel of Fig. 8 for the profile A–B–C, where the profile of  $|E_y|$  for the  $x$ -directed rods model (asterisks) matches the profile for the 0.0001 S m<sup>-1</sup> isotropic half-space (solid line passing through the asterisks).

The reason, we believe, for this close agreement is that  $|E_y|$  is generated by electric current flow in only the vertical and along-strike directions. Both of these directions have the same conductivity,  $\sigma_{\parallel}$ . In other words, EM fields diffusing along the strike of the anisotropy sample only the along-strike and vertical conductivities, which are the same. Thus, the along-strike electric field can be modelled by an isotropic half-space with conductivity  $\sigma_1 = \sigma_{\parallel}$ . On the other hand, the across-strike field strength  $|E_x|$  (as shown in Fig. 7a) cannot be modelled by

a simple isotropic half-space. The reason, we believe, is that EM fields diffusing across the strike of the anisotropy sample the across-strike and vertical conductivities, which in this case are different.

The paradox of anisotropy is seen clearly in Fig. 7(c), which shows that the total electric field strength is enhanced in the conductive ( $x$ ) direction. The enhancement effect is shown in Figs 7(c) and 8 for frequency 8 Hz, but the effect persists over the range of frequencies 1–128 Hz, as indicated in Fig. 9. The enhancement effect is negligible only at very low frequencies, such as 0.1 Hz and below, where the electric field strength for the  $x$ -directed rods model and the two half-space models are mutually indistinguishable from each other (Fig. 9, top left) and well approximated by the DC (zero-frequency) response.

The enhancement effect is shown again in Fig. 10, this time for a range of ‘ $x$ -directed rods’ models with anisotropy ratio varying from  $f = 1.0$  to  $f = 100$  (solid lines in the figure). The enhancement increases with the anisotropy ratio but is incompatible with an isotropic half-space response (dashed lines in the figure).

### The $y$ -directed dykes model

Consider now a uniaxial seafloor characterized by the electrical conductivity tensor  $\sigma = \text{diag}(\sigma_{\perp}, \sigma_{\parallel}, \sigma_{\parallel})$  with  $\sigma_{\parallel} > \sigma_{\perp}$ , which has the physical interpretation of  $y$ -directed conductive dykes impregnating an insulating matrix (top right of Fig. 3). This geometry is associated in the oceanic crust with preferentially aligned dykes and fractures.

The electric field strengths for the ‘ $y$ -directed dykes’ model with anisotropy ratio  $f = 0.1$  is shown in Fig. 11. Contours are shown for an anisotropic model (light solid lines) with  $\sigma_{\perp} = 0.0001 \text{ S m}^{-1}$  and  $\sigma_{\parallel} = 0.001 \text{ S m}^{-1}$ , along with those for an isotropic seafloor model (heavy dashed lines) with  $\sigma_1 = \sigma_{\parallel} = 0.001 \text{ S m}^{-1}$ . Note that the conductive direction is now along strike, in contrast to the  $x$ -directed rods model where the conductive direction was across strike.

From Fig. 11(a), it is again clear that the effect of the lateral anisotropy is to enhance the across-strike electric field  $|E_x|$  in the conductive direction. Again, this is opposite to what is naively expected based on isotropic theory. The effect is shown clearly in the bottom panel of Fig. 8: at the location  $x \sim 0$  halfway along the line B–C, the quantity  $|E_x|$  associated with the  $y$ -directed dykes model (filled circles) is *larger* than that associated with either of the background isotropic models. This is another example of the ‘paradox of anisotropy’.

From Fig. 11(b) it is evident that the along-strike electric field strength  $|E_y|$  contours for the  $y$ -directed dykes model (solid lines) follow almost exactly the field-strength contours for the isotropic half-space model (dashed lines), where the isotropic conductivity is  $\sigma_1 = \sigma_{\parallel} = 0.001 \text{ S m}^{-1}$ . This is clearly shown in the top panel of Fig. 8, where the profile of  $|E_y|$  for the  $y$ -directed dykes model (filled circles) matches the profile for the 0.001 S m<sup>-1</sup> isotropic half-space.

As before, the reason for this close agreement is that  $|E_y|$  is generated by electric current flow in only the vertical and along-strike directions. Both of these directions have the same conductivity. The across-strike field strength  $|E_x|$  (as shown in Fig. 11a) once again cannot be modelled by a simple isotropic half-space, since the EM diffusion paths between TX and RX sample differing across-strike and vertical conductivities.

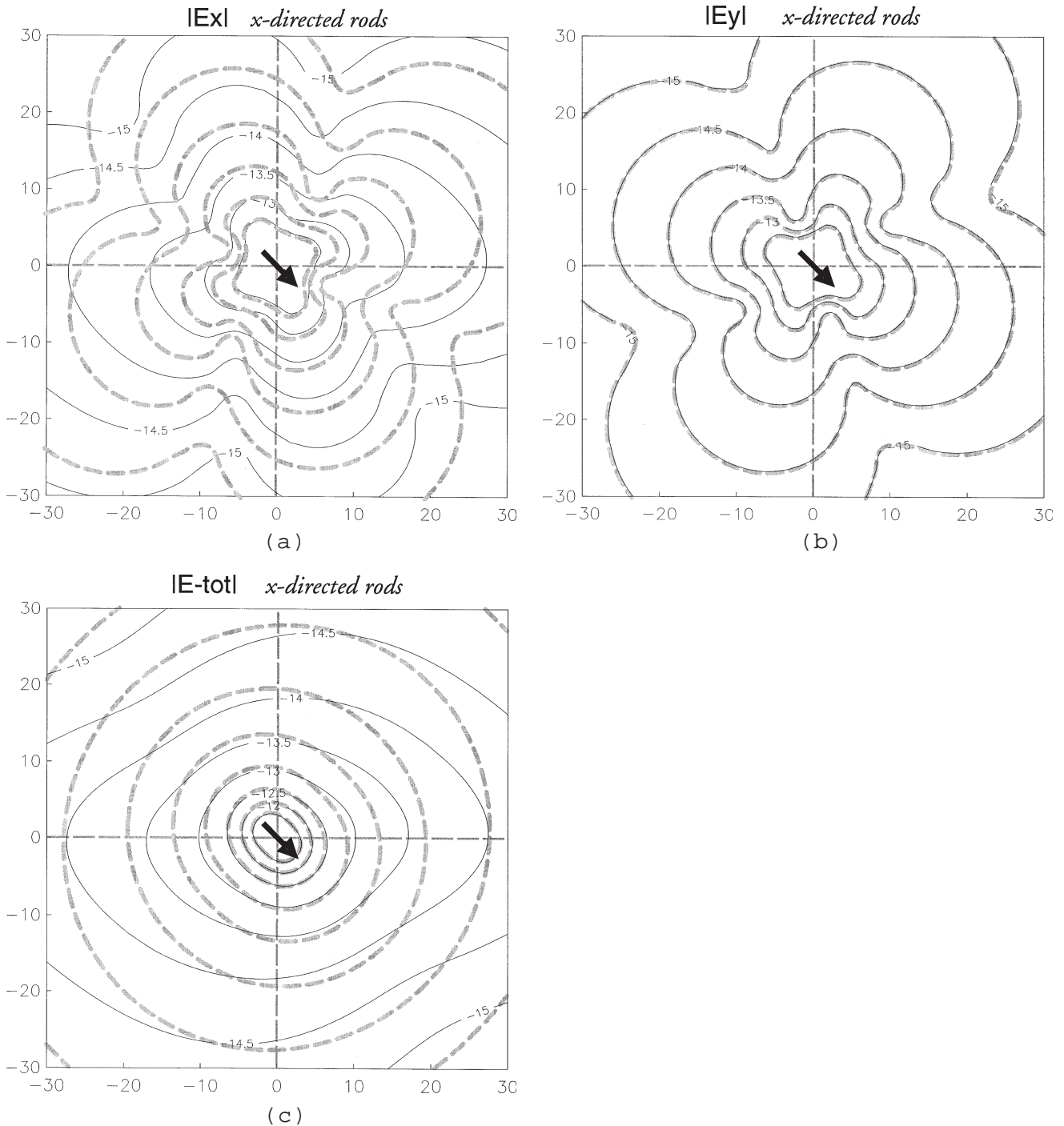


**Figure 7.** Logarithmically spaced contours (light solid lines) of the magnitude of (a) the across-strike electric field  $|E_x(x, y)|$ , (b) the along-strike electric field  $|E_y(x, y)|$ , and (c) the total horizontal electric field for 8 Hz excitation of an anisotropic 'x-directed rods' model with  $\sigma_{\perp} = 0.001 \text{ S m}^{-1}$  and  $\sigma_{\parallel} = 0.0001 \text{ S m}^{-1}$ . The along-strike electric field shown in (b) obeys the isotropic response (heavy dashed lines) of a  $0.0001 \text{ S m}^{-1}$  half-space. The across-strike and total electric fields for the anisotropic model are enhanced in the  $x$ -direction relative to the background isotropic response. This enhancement is a 'paradox of anisotropy', as explained in the text. Note that all the contour plots in this paper span an area of seafloor that is  $60 \text{ km} \times 60 \text{ km}$  and is centred on the transmitter. The abscissa is always the  $x$ -coordinate and the ordinate is always the  $y$ -coordinate (see Fig. 5), both of which range from  $-30$  to  $+30 \text{ km}$ .

The total electric field strength is again enhanced in the conductive ( $y$ ) direction, as indicated in Fig. 11(c). This 'paradox of anisotropy', modelled here in the frequency domain, has also been seen in the transient electric field (Yu & Edwards 1992, p. 440) for a  $y$ -directed dykes model with anisotropy ratio  $f = 0.25$ .

## DISCUSSION

Marine CSEM experiments are technically difficult and costly to perform. In addition, a quantitative interpretation of CSEM data in terms of the 2-D and 3-D geoelectrical structure of the seafloor generally involves complicated

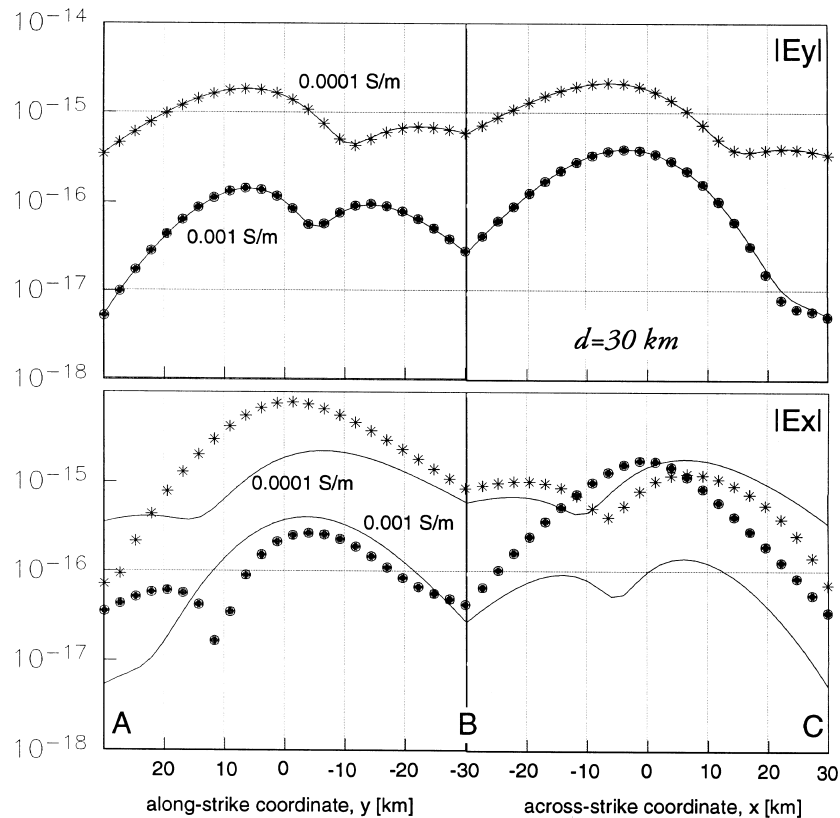


**Figure 8.** Profiles along lines A–B and B–C of the along-strike (top) and across-strike (bottom) electric field strengths, in  $\text{V m}^{-1}$ , for the ‘ $x$ -directed rods’ model (asterisks) and the ‘ $y$ -directed dykes’ model (filled circles). Also shown, as solid lines, are the electric field profiles for the two relevant background isotropic models of the seafloor. The orientation of the HED transmitter is in the direction  $\phi=135^\circ$ .

and time-consuming computer modelling. However, electromagnetic responses of such simple anisotropic structures as the uniaxial half-space have not yet received much attention in the marine geophysical literature. This is despite the fact that it is likely the seafloor exhibits a laterally anisotropic electrical signature.

The main finding of this paper has been the observation that the across-strike horizontal electric field is enhanced in the most conductive direction of a laterally anisotropic seafloor. The enhancement is evident for both the ‘ $x$ -directed rods’ and the ‘ $y$ -directed dykes’ models, and is contrary to what might be expected based on naive isotropic theory. Yu & Edwards (1992) previously found similar effects when studying the transient response of a ‘ $y$ -directed dykes’ model to excitation by an HED that is oriented perpendicular to the electrical strike direction. The results of the present paper indicate that the paradoxical ‘enhancement effect’ does not require a special orientation of the dipole transmitter: it holds for HED dipole moments oriented obliquely with respect to the electrical strike direction. For completeness and comparison with the previous work, the frequency-domain enhancement effect for an  $x$ -directed HED transmitter over the  $x$ -directed rods model ( $\sigma_{\perp}=0.001 \text{ S m}^{-1}$  and  $\sigma_{\parallel}=0.0001 \text{ S m}^{-1}$ ) is presented in Fig. 12.

The ‘paradox of anisotropy’ resists a simple explanation. The across-strike electric field component in the most conductive direction of the seafloor is simply larger than it ought to be, based on isotropic skin-effect arguments. To gain further insight into the paradox, it might be constructive to perform

2-D CSEM modelling on a seafloor consisting of a system of vertical conductive sheets impregnating an insulating matrix. As the density of vertical sheets is made large, and the thickness of individual sheets is made small, the ‘ $y$ -directed rods’ anisotropic model would be recovered. Investigating the behaviour of the electric fields as the 2-D isotropic model approaches the 1-D anisotropic model might well reveal the underlying cause of the ‘paradox of anisotropy.’

We have shown that the along-strike electric field over a laterally anisotropic seafloor can be modelled by an isotropic half-space, while the across-strike electric field cannot. Our explanation is that electric currents flowing along the strike of the electrical anisotropy sample only a single electrical conductivity, namely  $\sigma_{\parallel}$ . In contrast, electric currents flowing across the electrical strike sample two different conductivities:  $\sigma_{\perp}$  in the horizontal direction and  $\sigma_{\parallel}$  in the vertical direction. Our calculations are for a case where the skin depth in the sea water is much smaller than the skin depth in the seafloor, so that there is negligible electric current flow in the sea water. If the seafloor electrical conductivity is considerably higher, say approaching that of sea water, one would expect the along-strike electric field to be influenced also by  $\sigma_0$ , the sea-water conductivity. In that case, the interpretation of the along-strike electric field by a simple isotropic half-space might fail, since along-strike electric current flow would sample  $\sigma_0$  in addition to  $\sigma_{\parallel}$ . However, as indicated in Fig. 13, the interpretation of along-strike electric field by an isotropic half-space remains valid for seafloor electrical conductivities as large as 0.1 and

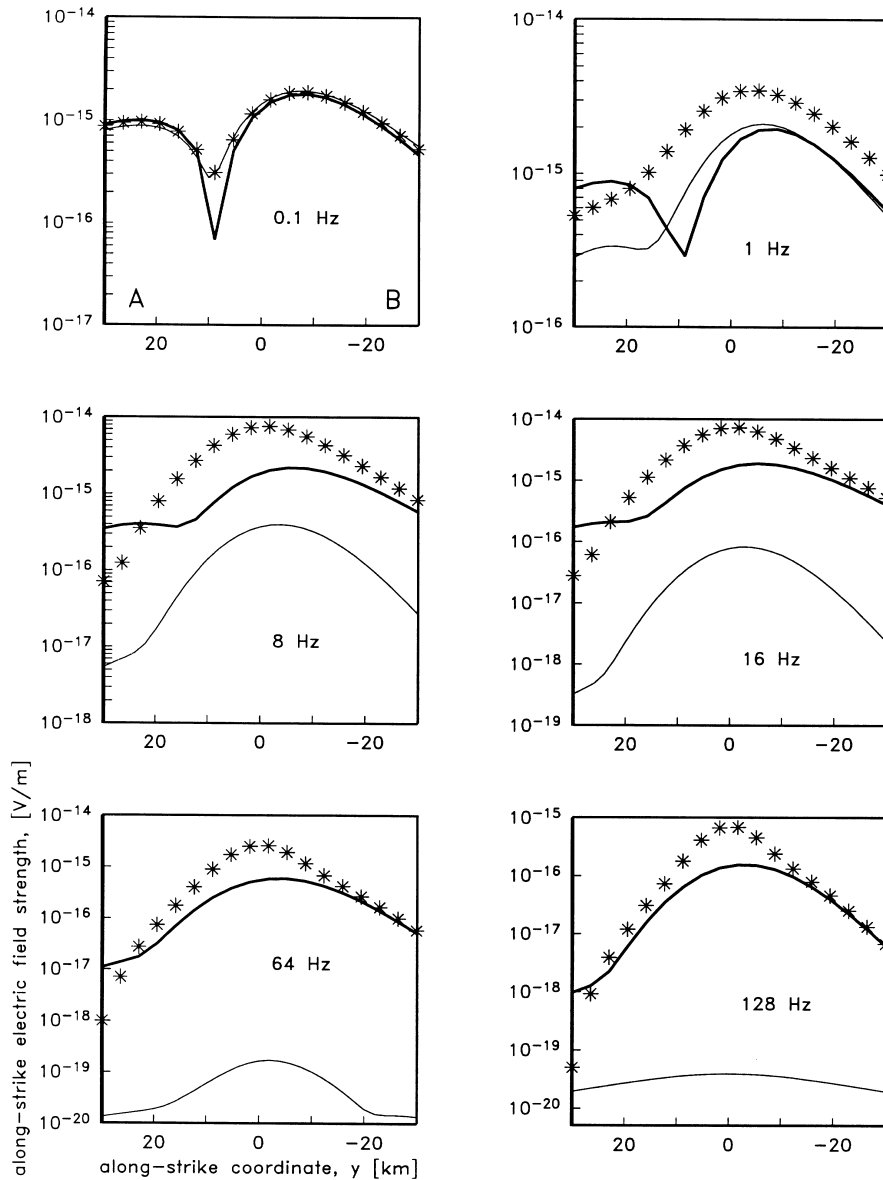


**Figure 9.** Across-strike electric field strength  $|E_x|$  along the profile A–B for the ‘ $x$ -directed rods’ model (asterisks) and the two relevant background isotropic models,  $\sigma_1 = 0.001 \text{ S m}^{-1}$  (light line) and  $\sigma_1 = 0.0001 \text{ S m}^{-1}$  (heavy line). The field strength is shown as a function of frequency for the range 0.1–128 Hz.

$0.01 \text{ S m}^{-1}$ , which is two orders of magnitude more conductive than those considered earlier in this paper.

Our results also indicate that the along-strike electrical conductivity can be extracted from marine CSEM data more readily than the across-strike electrical conductivity. The latter requires full anisotropic modelling. The former requires just isotropic modelling, provided the seafloor electric fields have been decomposed into components that are oriented parallel and perpendicular to the strike of the anisotropy. Presumably, the ability to extract along-strike conductivity using isotropic modelling is not restricted to simple half-space models but could be extended to layered or smooth models, as long as the strike direction of the anisotropy is invariant with depth. However, the difficulty of performing this decomposition in practice is that the strike direction of the seafloor, if there is one, is generally uncertain.

#### APPLICATION TO PEGASUS DATA

We now return to the data that motivated this study (Fig. 1, right), which are characterized by relatively attenuated E–W electric fields both along and across strike from the transmitter. The two models we originally considered to be candidates for marine anisotropy, mantle ‘ $x$ -directed rods’ (ridge-perpendicular lineations) and crustal ‘ $y$ -directed dykes’ (ridge-parallel dykes and faults), fail to fit the observations. The  $x$ -directed rods model, for example, produces larger  $|E_x|$  than  $|E_y|$  in the across-strike direction but similar amplitudes for both in the along-strike direction. The  $y$ -directed dykes model produces larger  $|E_x|$  than  $|E_y|$  in the along-strike direction but similar amplitudes for both in the across-strike direction. If the ridge-parallel (N–S) dykes or ridge-perpendicular (E–W) mantle lineations are geologically reasonable structures, then

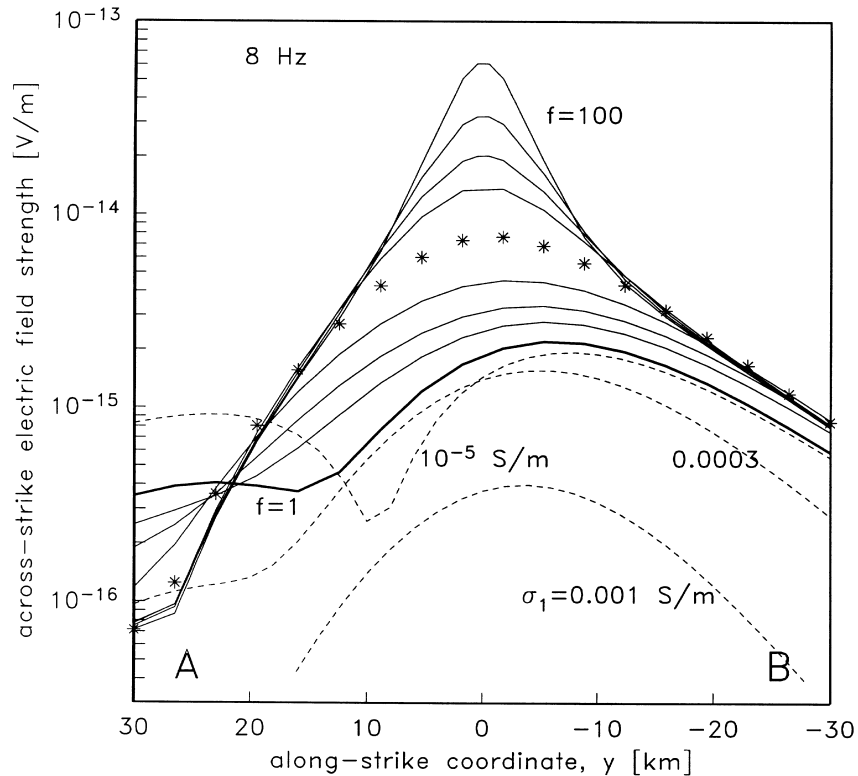


**Figure 10.** Across-strike electric field strength  $|E_x|$  along the profile A–B for ‘ $x$ -directed rods’ models with varying ratios of anisotropy,  $f = \sigma_{\perp} / \sigma_{\parallel}$ . The heavy solid line is the isotropic response ( $f=1$ ) for  $\sigma_1 = 0.0001 \text{ S m}^{-1}$ . The light solid lines are the responses for various values of  $f$ , increasing upwards to  $f=100$ . The asterisks are the response for the anisotropic model with  $f=10$ . The dashed lines are isotropic responses, with lower-half-space electrical conductivities as indicated.

we have the additional problem that the simple modelling predicts an enhancement of the E–W components only, not the N–S components as observed.

Fortunately, simple anisotropic half-space modelling is not yet exhausted: ‘ $x$ -directed dykes’ (ridge-perpendicular dykes or faults) and ‘ $y$ -directed rods’ (ridge-parallel lineations) are calculable by rotating the mathematical construct clockwise by  $90^\circ$ . We now find that not only is a qualitative fit possible with a ridge-perpendicular dyke model (the middle right structure portrayed in Fig. 3), but a good quantitative fit is possible (Fig. 14) for a model with  $\sigma_{\text{NS}} = 0.0001 \text{ S m}^{-1}$  and  $\sigma_{\text{EW}} = 0.0007 \text{ S m}^{-1}$ , where  $\sigma_{\text{NS}}$  is the electrical conductivity in the N–S direction parallel to the fossil ridge while  $\sigma_{\text{EW}}$  is the electrical conductivity in the E–W direction perpendicular to the fossil ridge. Accordingly, our best-fitting model is most conductive in the E–W direction. (Note that  $\sigma_{\text{NS}}$  is equivalent to  $\sigma_{\perp}$  in the notation of Fig. 3, and  $\sigma_{\text{EW}}$  is equivalent to  $\sigma_{\parallel}$ .)

The preferred model fits all the data within two error bars. This is true for instrument Macques, even though the logarithmic scale makes the misfit appear poor. In any case, the datum for this instrument is very close to the noise threshold (Constable & Cox 1996, Fig. 5) and probably represents only an upper limit on signal strength at this location; the predicted field of  $4 \times 10^{-19} \text{ V m}^{-1} (\text{Am})^{-1}$  could never be measured in this experiment.

Although we are presently restricted to half-space modelling, we can argue that our observed anisotropy is within the uppermost mantle. Previous isotropic modelling of this data set (Constable & Cox 1996) has indicated that at least a

two-layered isotropic structure is required, and our attempts to decompose the short-range two-component data (the ‘ELFs’ of Fig. 1) into N–S and E–W components demonstrates that the ‘amplitude split’ (which is diagnostic of anisotropy) disappears at ranges of less than about 20 km. Both suggest that a model of an isotropic crust over an anisotropic mantle is appropriate.

Our preferred electrical model is, perhaps, a geologically reasonable representation of mantle structure, even though our expected physical model for mantle anisotropy was for ridge-perpendicular lineations (top left diagram of Fig. 3) rather than the ‘dykes’ (middle right diagram of Fig. 3) that we found. Because the scale of our experiment precludes our ability to distinguish between anisotropy due to mineralogical fabric and structures several kilometres in size, along-axis variations in ridge chemistry might imprint along-axis variations in electrical conductivity on the depleted oceanic mantle during seafloor spreading, thus creating a macro-anisotropy with a resistive ridge-parallel component. More persuasively, perhaps, dipping ridge-perpendicular lineations of conductive minerals would enhance conductivity in both vertical and ridge-perpendicular directions, just as our mathematical model requires. Such dipping lineations are characteristic of the mantle flow models of McKenzie (1979) and Blackman *et al.* (1996), and might be manifest either as true micro-anisotropy associated with crystal alignment and/or grain boundary phases, or as a macro-anisotropic distribution of minerals along the strain direction.

We consider various ways in which an anisotropic mantle fabric could generate an electrical signature. Mantle seismic

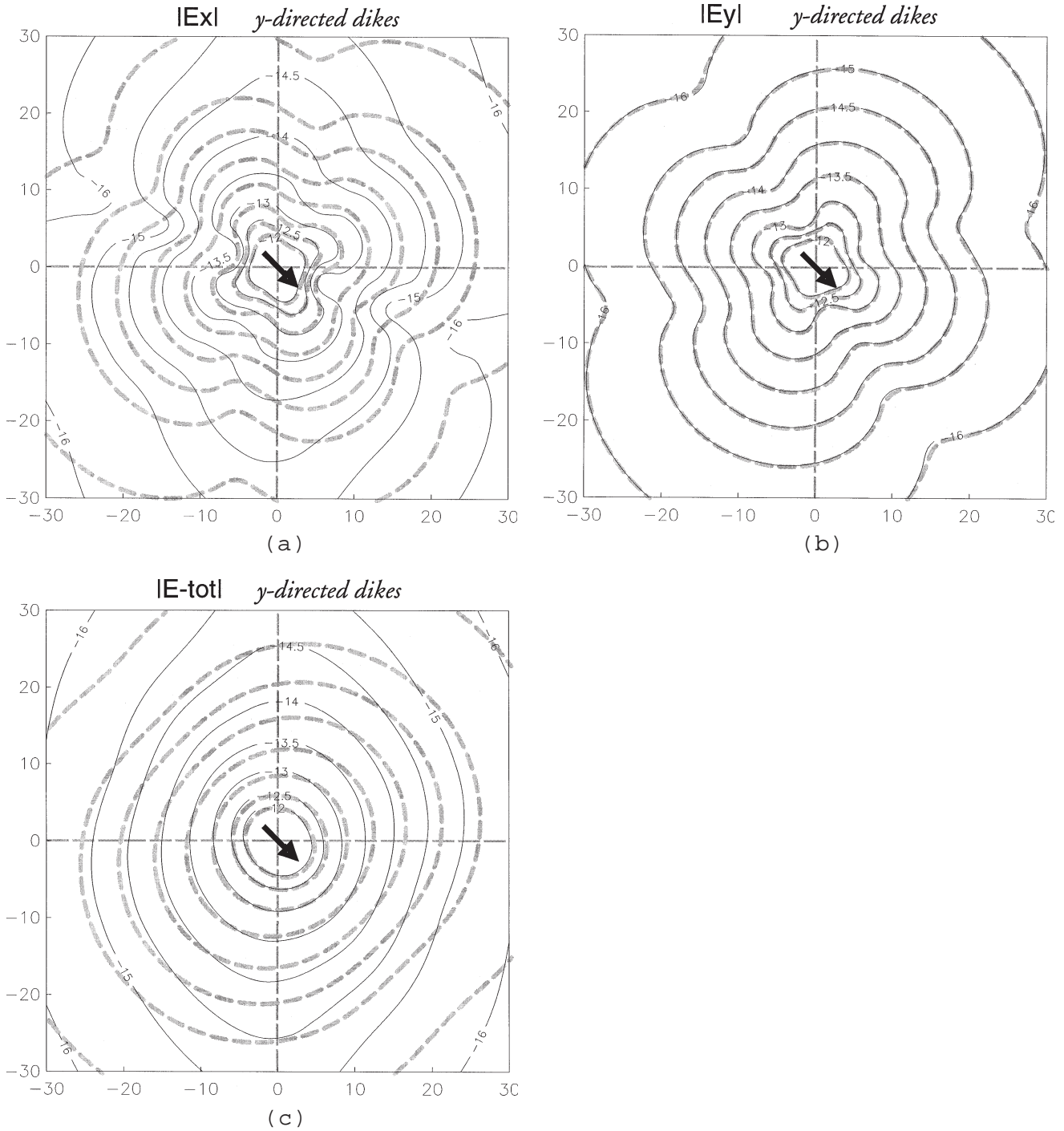


**Figure 11.** Logarithmically spaced contours (light solid lines) of the magnitude of (a) the across-strike electric field  $|E_x(x, y)|$ , (b) the along-strike electric field  $|E_y(x, y)|$ , and (c) the total horizontal electric field for 8 Hz excitation of an anisotropic ‘ $y$ -directed dykes’ model with  $\sigma_{\perp} = 0.0001 \text{ S m}^{-1}$  and  $\sigma_{\parallel} = 0.001 \text{ S m}^{-1}$ . The along-strike electric field shown in (b) obeys the isotropic response (heavy dashed lines) of a  $0.001 \text{ S m}^{-1}$  half-space. The across-strike and total electric fields for the anisotropic model are enhanced in the  $y$ -direction relative to the background isotropic response. This enhancement is a ‘paradox of anisotropy’, as explained in the text.

anisotropy is generally attributed to the preferred alignment of the  $a$ -axis in olivine grains. This can be eliminated as the cause of electrical anisotropy. The data respond to conductivity only above about 40 km depth, where temperatures are below  $800 \text{ }^{\circ}\text{C}$  and too low for dry olivine conduction to dominate. Additionally,  $a$ -axis conduction is intermediate between  $b$ - and

$c$ -axis conduction, which themselves differ only by a factor of 3—too little to explain our observations of at least a factor of 7.

Conduction by mantle hydrogen (Karato 1990) presents an interesting possible explanation of our results. In this case, the  $a$ -axis in olivine is predicted to be the most efficient conductive

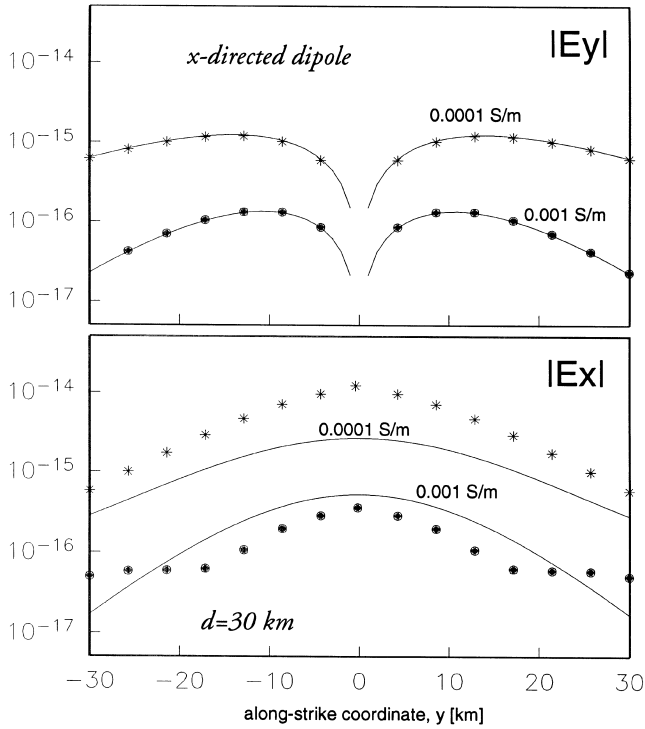


**Figure 12.** Profiles along line A–B of the along-strike (top) and across-strike (bottom) electric field strengths, in  $V\ m^{-1}$ , for the ‘x-directed rods’ model (asterisks) and the ‘y-directed dykes’ model (filled circles). Also shown, as solid lines, are the electric field profiles for the two relevant background isotropic models of the seafloor. The orientation of the HED transmitter is in the positive  $x$ -direction,  $\phi = 90^\circ$ .

path. The conductivities predicted by Karato (1990) imply that our conductivity of  $\sigma_{EW} = 0.0007\ S\ m^{-1}$  could be achieved below  $800\ ^\circ C$  with hydrogen to silicon ratios between 100 and 1000 ppm. Hydrogen diffusion along the  $a$ - and  $c$ -axes differs

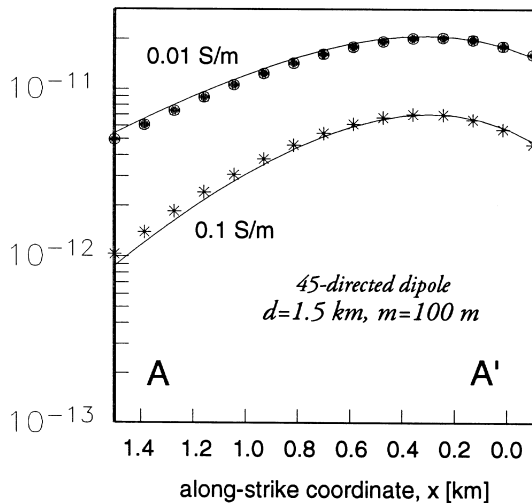


**Figure 13.** Profile along line A–A’ of the across-strike electric field strength, in  $V\ m^{-1}$ , for very conductive ‘x-directed rods’ (asterisks) and ‘y-directed dykes’ (filled circles) models. Also shown, as solid lines, are the electric field profiles for the two relevant background isotropic models of the seafloor. The orientation of the HED transmitter is in the direction  $\phi = 135^\circ$ .

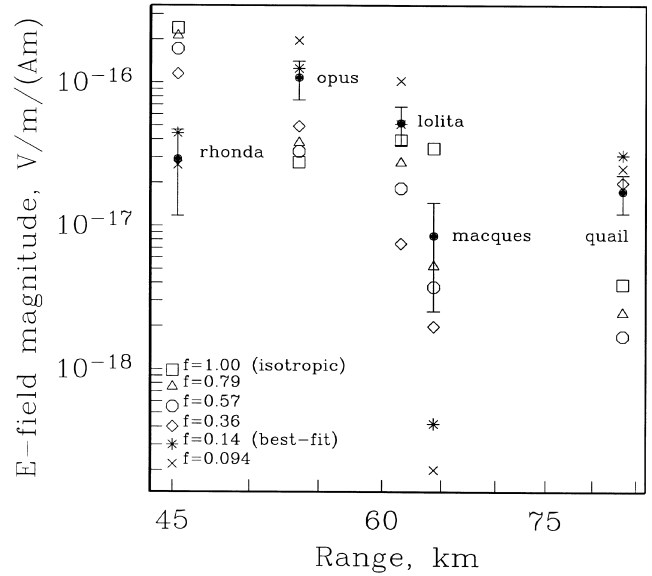


**Figure 14.** The responses of some ‘x-directed dykes’ electrical conductivity models plotted against the observed PEGASUS electric field magnitudes (solid circles). An ‘x-directed dyke’ model has the structure shown in the middle right diagram of Fig. 3. The responses shown here were calculated by rotating clockwise through  $90^\circ$  the responses of equivalent ‘y-directed dyke’ models. Six different anisotropic models were examined with various anisotropic ratios  $f = \sigma_{NS} / \sigma_{EW}$ , ranging from  $f = 0.094$  to isotropic ( $f = 1.00$ ). The isotropic model (response indicated by the square symbols) is  $\sigma_{NS} = \sigma_{EW} = 0.00026\ S\ m^{-1}$ , and represents the best-fitting isotropic half-space. The other five models were constructed by decreasing the anisotropic ratio  $f$  while keeping the geometric mean conductivity  $\sqrt{\sigma_{NS}\sigma_{EW}}$  constant. The best fit was obtained for  $f = 0.14$  (asterisks), which corresponds to a N–S electrical conductivity of  $\sigma_{NS} = 0.0001\ S\ m^{-1}$  and an E–W electrical conductivity of  $\sigma_{EW} = 0.0007\ S\ m^{-1}$ . The possible geological implications of this result are discussed in the text.

by an order of magnitude, and so our factor of 7 anisotropy is consistent with a dipping lineation direction or less than complete alignment. Some of the concerns expressed by Constable (1993), directed at the application of hydrogen conduction to the deeper, more conductive mantle, still stand. It has not yet been demonstrated that hydrogen forms a charge carrier in olivine (Karato’s work was based on diffusion, rather than conductivity, measurements), and hydrogen in the mantle may preferentially partition into pyroxene.

Conduction by a grain boundary phase, such as carbon or magnetite, will be susceptible to an anisotropy induced by rock fabric. For example, preferential alignment of the  $a$ -axis in tabular olivine grains produces lineations in the flow direction. However, typical crystal aspect ratios are less than we require for our observations. Much larger anisotropies are created by deformation-induced accumulations of conductive minerals (e.g. Jones *et al.* 1997). McKenzie’s (1979) and Blackman *et al.*’s (1996) models of fluid flow during seafloor spreading both predict strain ellipses with aspect ratios of 10:1 or more. Graphite, magnetite or other conductive oxides and sulphides that have been redistributed along strain directions during seafloor spreading but retain some grain-to-grain contact could easily explain our observed anisotropy. The low activation energies of conductors such as carbon and magnetite are ideal for explaining conductivities at low uppermost-mantle

temperatures, and they are only required in trace amounts. Both minerals have conductivities of the order of  $10^5 \text{ S m}^{-1}$  (Duba & Shankland 1982; Telford *et al.* 1990), and so concentrations of only  $10^{-8}$  as a connected phase are needed to satisfy our observations; no doubt more exists as discrete grains.

## CONCLUDING COMMENTS

The modelling results presented here offer considerable physical insight into frequency-domain electromagnetic induction in uniaxial media. Even though our present modelling capability is restricted to anisotropic half-space structures, qualitative insights are certainly helpful when interpreting marine CSEM experimental data, and in spite of the limitations a good quantitative fit to long-range CSEM data from the PEGASUS experiment can be obtained. Our model of enhanced conductivities in the vertical and ridge-perpendicular directions is consistent with alignment and/or distribution of minerals by the strain field associated with seafloor spreading processes. Results such as these, based on only five data points, beg the question of verification. Further controlled-source experiments would certainly be desirable, but since the depths of investigation are at the limit of what can be achieved with CSEM methodology, the magnetotelluric (MT) method should also be considered. That previous MT experiments have not observed this anisotropy is no surprise; the depths are too shallow and the resistivities too high for long-period MT studies to be affected. Application of high-frequency MT, developed for petroleum exploration (Constable *et al.* 1998), might well be the most appropriate tool to verify our result.

## ACKNOWLEDGMENTS

This work was completed during a visit by ME to Scripps Institution of Oceanography during the summer of 1997. The authors thank Martin Sinha, Nigel Edwards, Lucy MacGregor, Liming Yu and Xiaobo Li for interesting discussions, and particularly appreciate helpful reviews from Colin Farquharson and Martyn Unsworth.

## REFERENCES

- Blackman, D.K., Kendall, J.-M., Dawson, P.R., Wenk, H.-R., Boyce, D. & Phipps Morgan, J., 1996. Teleseismic imaging of subaxial flow at mid-ocean ridges: traveltimes effects of anisotropic mineral texture in the mantle, *Geophys. J. Int.*, **127**, 415–426.
- Cairns, G., Evans, R.L. & Edwards, R.N., 1996. A transient electromagnetic survey of the TAG hydrothermal mound, *Geophys. Res. Lett.*, **23**, 3455–3458.
- Chave, A.D., 1983. Numerical integration of related Hankel transforms by quadrature and continued fraction expansion, *Geophysics*, **48**, 1671–1686.
- Chave, A.D. & Cox, C.S., 1982. Controlled electromagnetic sources for measuring electrical conductivity beneath the oceans. I. Forward problem and model study, *J. Geophys. Res.*, **87**, 5327–5338.
- Cheesman, S.J., Edwards, R.N. & Chave, A.D., 1987. On the theory of seafloor conductivity mapping using transient electromagnetic systems, *Geophysics*, **52**, 204–217.
- Cheesman, S.J., Law, L.K. & St. Louis, B., 1993. A porosity mapping survey in Hecate Strait using a seafloor electromagnetic profiling system, *Marine Geol.*, **110**, 245–256.
- Clemmow, P.C., 1963. The theory of electromagnetic waves in a simple anisotropic medium, *Proc. I.E.E.*, **110**, 101–106.
- Constable, S. & Cox, C.S., 1996. Marine controlled-source electromagnetic sounding 2. The PEGASUS experiment, *J. geophys. Res.*, **101**, 5519–5530.
- Constable, S., Orange, A., Hoversten, G.M. & Morrison, H.F., 1998. Marine magnetellurics for petroleum exploration 1. A seafloor instrument system, *Geophysics*, **63**, 816–825.
- Constable, S.C., 1993. Conduction by mantle hydrogen, *Nature*, **362**, 704.
- Constable, S.C., Parker, R.L. & Constable, C.G., 1987. Occam's inversion: a practical algorithm for generating smooth models from electromagnetic sounding data, *Geophysics*, **52**, 289–300.
- Cox, C.S., Constable, S.C., Chave, A.D. & Webb, S.C., 1986. Controlled-source electromagnetic sounding of the oceanic lithosphere, *Nature*, **320**, 52–54.
- Evans, R.L., Sinha, M.C., Constable, S.C. & Unsworth, M.J., 1994. On the electrical nature of the axial melt zone at  $13^\circ\text{N}$  on the East Pacific Rise, *J. geophys. Res.*, **99**, 577–588.
- Evans, R.L., Law, L., St. Louis, B., Cheesman, S. & Sananikone, K., 1997. The shallow porosity structure of the continental shelf off Humboldt Bay, California: results of a towed electromagnetic survey, in *SAGEEP'97: Symposium on the Application of Geophysics to Engineering and Environmental Problems*, pp. 937–946, March 23–26, Reno, NV.
- Everett, M.E. & Edwards, R.N., 1992. Transient marine electromagnetics: The 2.5-D forward problem, *Geophys. J. Int.*, **113**, 545–561.
- Duba, A. & Shankland, T.J., 1982. Free carbon and electrical conductivity in the Earth's mantle, *Geophys. Res. Lett.*, **9**, 1271–1274.
- Flosadottir, A.H. & Constable, S., 1996. Marine controlled-source electromagnetic sounding 1. Modelling and experimental design, *J. geophys. Res.*, **101**, 5507–5517.
- Jones, A.G., Katsube, T.J. & Schwann, P., 1997. The longest conductivity anomaly in the world explained: sulphides in fold hinges causing high electrical anisotropy, *J. Geomag. Geoelectr.*, **49**, 1619–1629.
- Karato, S., 1990. The role of hydrogen in the electrical conductivity of the upper mantle, *Nature*, **347**, 272–273.
- Kaufmann, A.A. & Keller, G.V., 1983. *Frequency and Transient Sounding*. Elsevier, Amsterdam.
- Le Masne, D. & Vasseur, G., 1981. Electromagnetic field of sources at the surface of a homogeneous conducting halfspace with horizontal anisotropy: application to fissured media, *Geophys. Prospect.*, **29**, 803–821.
- Li, X. & Pedersen, L.B., 1991. The electromagnetic response of an azimuthally anisotropic half-space, *Geophysics*, **56**, 1462–1473.
- MacGregor, L.M., Constable, S. & Sinha, M.C., 1998. The RAMESSES experiment—III. Controlled-source electromagnetic sounding of the Reykjanes Ridge at  $57^\circ 45'\text{N}$ , *Geophys. J. Int.*, **135**, 773–789.
- McKenzie, D., 1979. Finite deformation during fluid flow, *Geophys. J. R. astr. Soc.*, **58**, 689–715.
- Shearer, P. & Orcutt, J., 1985. Anisotropy in the oceanic lithosphere: theory and observations from the Ngendie seismic refraction experiment in the southwest Pacific, *Geophys. J. R. astr. Soc.*, **80**, 493–526.
- Sinha, M.C., Patel, P.D., Unsworth, M.J., Owen, T.R.E. & MacCormack, M.R.G., 1990. An active source electromagnetic sounding system for marine use, *Marine Geophys. Res.*, **12**, 59–68.
- Sinha, M.C., Constable, S.C. & MacGregor, L.M., 1996. Controlled source electromagnetic sounding of the Valu Fa back-arc spreading ridge in the Lau Basin, SW Pacific, in *13th Workshop on Electromagnetic Induction in the Earth*, p. 49, July 12–18, Onuma, Japan (abstract).

- Telford, W.M., Geldart, L.P. & Sheriff, R.E., 1990. *Applied Geophysics*, Cambridge University Press, Cambridge.
- Unsworth, M.J. & Oldenburg, D., 1995. Subspace inversion of electromagnetic data: application to mid-ocean ridge exploration, *Geophys. J. Int.*, **123**, 161–168.
- Unsworth, M.J., Travis, B.J. & Chave, A.D., 1993. Electromagnetic induction by a finite electric dipole source over a 2-D earth, *Geophysics*, **58**, 198–214.
- Xiong, Z., 1989. Electromagnetic fields of electric dipoles embedded in a stratified anisotropic earth, *Geophysics*, **54**, 1643–1646.
- Young, P.D. & Cox, C.S., 1981. Electromagnetic active source sounding near the East Pacific Rise, *Geophys. Res. Lett.*, **8**, 1043–1046.
- Yu, L. & Edwards, R.N., 1992. The detection of lateral anisotropy of the ocean floor by electromagnetic methods, *Geophys. J. Int.*, **108**, 433–441.
- Yu, L., Evans, R.L. & Edwards, R.N., 1997. Transient electromagnetic responses in seafloor with triaxial anisotropy, *Geophys. J. Int.*, **129**, 292–304.
- Zhang, S. & Karato, S., 1995. Lattice preferred orientation of olivine aggregates deformed in simple shear, *Nature*, **375**, 774–777.